New methodology to estimate Arctic sea ice concentration from SMOS combining brightness temperature differences in a maximum likelihood estimator

Carolina Gabarro[1], Antonio Turiel[1], Pedro Elosegui[1,2], Joaquim A. Pla-Resina[1], and Marcos Portabella[1]

[1]Barcelona Expert Center, Institute of Marine Sciences, ICM/CSIC, Passeig Maritim Barceloneta 39, Barcelona, Spain.
[2]Massachusetts Institute of Technology, Haystack Observatory, Westford, MA, USA.

Correspondence to: Carolina Gabarro (cgabarro@icm.csic.es)

Abstract.

Monitoring sea ice concentration is required for operational and climate studies in the Arctic Sea. Technologies used so far for estimating sea ice concentration have some limitations, as for instance the impact of the atmosphere, the physical temperature of ice, the presence of snow and melting, etc. In the last years, L-band radiometry has been successfully used to study some properties of sea ice, remarkably sea ice thickness. However, the potential of satellite L-band observations for obtaining sea ice concentration had not yet been explored.

In this paper, we present preliminary evidence showing that data from Soil Moisture Ocean Salinity (SMOS) mission can be used to estimate sea ice concentration. Our method, based on a Maximum Likelihood Estimator (MLE), exploits the marked difference in the radiative properties of sea ice and seawater. In addition, the brightness temperatures of 100% sea ice and 100% sea water, as well as their combined values (polarization and angular difference), have been shown to be very stable during winter and spring, so they are robust in front of variations in physical temperature and other geophysical parameters. Therefore, we can use just two set of tie points, one for summer and another for winter, for calculating sea ice concentration, leading to a more robust estimate.

After analysing the full year 2014 in the entire Arctic, we have found that the sea ice concentration obtained with our method is well determined as compared to Ocean and Sea Ice Satellite Application Facility (OSI-SAF) dataset. However, when thin sea ice is present (ice thickness $\lesssim 0.6$ m) the method underestimates the actual sea ice concentration.

Our results open the way for a systematic exploitation of SMOS data for monitoring sea ice concentration, at least for specific seasons. Additionally, SMOS data can be synergistically combined with data from other sensors to monitoring of pan-Arctic sea ice conditions.

1 Introduction

The Arctic Ocean is under profound transformation. The rapid decline in Arctic sea ice extent and volume that is both observed and modeled (e.g., Comiso, 2012; Stroeve et al., 2012) may have become the key illustration of change in a warming planet, but change is widespread across the whole Arctic system (e.g., AMAP, 2012; IPCC, 2013; SEARCH, 2013). A retreating

5 Arctic sea ice cover has a marked impact on regional and global climate, and vice versa, through a large number of feedback mechanisms and interactions with the climate system (e.g., Holland and Bitz, 2003; Cohen et al., 2014; Vihma, 2014).

The launch of the Soil Moisture and Ocean Salinity (SMOS) satellite, in 2009, marked the dawn of a new type of space-based microwave imaging sensor. Originally conceived to map geophysical parameters of both hydrological and oceanographic interest (e.g., Martin-Neira et al., 2002; Mecklenburg et al., 2009), SMOS is also making serious inroads in the cryospheric

10 sciences (e.g., Kaleschke et al., 2010, 2012; Huntemann et al., 2014). Developed by the European Space Agency (ESA), SMOS single payload, called Microwave Imaging Radiometer using Aperture Synthesis (MIRAS), is an L-band (1.4 GHz, or 21-cm wavelength) passive interferometric radiometer that measures the electromagnetic radiation emitted by Earth's surface. The observed brightness temperature (T_B) can be related to moisture content over the soil and to salinity over the ocean surface (Kerr et al., 2010; Font et al., 2013), as can be used to infer sea ice thickness (Kaleschke et al., 2012) and snow thickness

15 (Maaß, 2013; Maaß et al., 2015).

Sea ice concentration (SIC), defined as the fraction of ice relative to the total area at a given ocean location, is often used to determine other important climate variables such as ice extent and ice volume. SIC has been the target of satellite-based passive microwave sensors such as the Special Sensor Microwave/Imager (SSM/I and SSMIS) and the Advanced Microwave Scanning Radiometer (AMSR-E and AMSR-2) for more than 30 years. SIC can be estimated due to the fact that the brightness

20 temperature of sea ice and seawater are quite distinct. There exists a variety of algorithms to retrieve SIC from T_B observations tuned to those higher-frequency sensors, that is frequencies between 6–89 GHz (e.g., Cavalieri et al., 1984; Comiso, 1986; Ramseier, 1991; Smith, 1996; Markus and Cavalieri, 2000; Kaleschke et al., 2001; Shokr et al., 2008). Those algorithms present different advantages and drawbacks depending on frequency, spatial resolution, atmospheric effects, physical temperature, and others. According to Ivanova et al. (2015), the first source of error in the computation of sea ice concentration is the sensitivity

25 to changes in the physical temperature of sea ice, in particular for those algorithms that use measurements between 10–37 GHz. They identify atmospheric water vapor and cloud liquid water as the second source of error except for algorithms at 89 GHz, where it becomes the dominant error. Another problem faced by higher frequency radiometers is that the SIC retrievals are affected by the thickness of snow cover, which is difficult to determine.

Wilheit (1978) analyzed the sensitivity of microwave emissivity of open seawater to a variety of geophysical variables such

30 as atmospheric water vapor, sea surface temperature, wind speed, and salinity as function of frequency (Figure 1). The figure illustrates that L-band (1-2 GHz) observations are in a sweet spot, with the effect of all variables but salinity being minimal around the SMOS frequency. The same authors also showed that the signature of multi-year (MY) and first-year (FY) ice overlap in the lower microwave frequencies, while this is not the case at higher frequencies.

Although some authors (e.g., Mills and Heygster, 2011a; Kaleschke et al., 2013) have recently explored the feasibility of SIC determination using an aircraft-mounted L-band radiometer, a method that extends satellite-based SIC retrievals down to L-band (i.e., SMOS) frequencies has been missing. We therefore set out to develop a new method, which we present here.

A significant difference between high-frequency and L-band microwave radiometry is that ice penetration at L-band is non-negligible (Heygster et al., 2014). In other words, ice is more transparent (i.e., optically thinner) at low than at high microwave frequencies. As a consequence, the brightness temperature measured by an L-band antenna is not only emitted by the topmost ice surface layer but by a larger range of deeper layers within the ice. Thanks to that increased penetration in sea ice (about 60 cm depending on ice conditions), the SMOS L-band radiometer is also sensitive to ice thickness (Kaleschke et al., 2012; Huntemann et al., 2014).

We exploit some of SMOS observational features in this study to develop a new method to estimate SIC. These include a combination of acquisition modes involving dual and full polarization, continuous multiangle viewing between nadir and $65°$, wide swath of about 1200 km, spatial resolution of 35-50 km, and 3-day revisit time at the equator but more frequently at the poles. In particular, the multiangle viewing capability of SMOS is a noteworthy feature; it means that the same location on the Earth's surface can be observed quasi-simultaneously from a continuous range of angles of incidence as the satellite overpasses it.

The new method we present in this paper uses SMOS brightness temperature observations T_B and a Maximum Likelihood Estimator (MLE) to obtain SIC maps in the Arctic Ocean. We describe SMOS data and a radiative transfer model for sea ice that allows us to compute its emissivity, in Sections 2 and 3, respectively. We then introduce the concept of tie-points and its sensitivity to different geophysical parameters to help with SIC retrievals via algorithmic inversion of SMOS data, in Section 4.1, 4.2, 4.3, and 4.4, and the MLE inversion algorithm, in Section 4.5. We then perform an accuracy assessment of SIC estimates using SMOS by comparing them to an independent SIC dataset, in Section 5, to close with a discussion and conclusions, in Section 6 and 7, respectively.

2 Data

2.1 SMOS data from the Arctic Ocean

Since its launch in 2009, ESA has been generating brightness temperature full-polarization data products from SMOS. In this study, we focus on the official SMOS Level 1B (L1B) product version 504 data north of $60°$ N from 2014 to estimate SIC. The L1B data contains the Fourier components of T_B at the antenna reference frame (Deimos, 2010), from which one can obtain temporal snapshots of the spatial distribution of T_B (i.e., an interferometric T_B image) by performing an inverse Fourier transform. The T_B data are geo-referenced at an Equal-Area Scalable Earth (EASE) Northern hemisphere grid (Brodzik and Knowles, 2002) of 25 km on the side. The radiometric accuracy of individual T_B observations from SMOS is $\sim$2 K at boresight, and it increases on the Extended Alias Free Field-of-View (Corbella et al., 2011). Proceeding from L1B data, though computationally more demanding than the more traditional L1C data products, has several benefits. For example, it allows one to change the antenna grid from the operational size of 128x128 pixels to 64x64 pixels. As shown by Talone et al. (2015), the

smaller grid is optimal in that it helps mitigate some of the spatial correlations between measurements that are present in the larger grid.

We correct T_B for a number of standard contributions such as geomagnetic and ionospheric rotation and atmospheric attenuation (Zine et al., 2008). The galactic reflection is not significant at high latitudes, and no correction was applied. We then
5   filter out outliers (defined as those estimates that deviate by more than 3-σ from the mean value, where σ is the radiometric accuracy at the given point in the antenna plane) and filtered out T_B observations in regions of the field of view that are known to have low accuracy due to aliasing (Camps et al., 2005), Sun reflections, and Sun tails.

To lower the noise level, we averaged T_B measurements from both ascending and descending orbits over periods of 3 days, which thus define the time resolution of our SIC maps. We also averaged acquisitions in incidence angle binnings of 2°. Since
10   some incidence angles could be missing due to the SMOS acquisition feature and interferences, we use a cubic polynomial fit to interpolate T_B measurements to have the full range of incidence angles in each grid position.

2.2   OSI-SAF and other sea ice data products

We use SIC maps from the database of the Ocean and Sea Ice Satellite Application Facility (OSI SAF product version OSI-401a) of the European Organization for the Exploitation of Meteorological Satellites (EUMETSAT) for comparison with the
15   products we are obtaining.

These are computed from brightness temperature observations from SSMIS at 19 and 37 GHz, are corrected for atmospheric effects using forecasts from the European Center for Medium Range Weather Forecasts (ECMWF), use monthly dynamic tie-points, are available on polar Stereographic 10-km grid for both polar hemispheres, and include SIC uncertainty estimates (Tonboe et al., 2016). In this study, we used daily SIC maps in the Arctic Ocean from the OSI-SAF northern hemisphere
20   products of the year 2014.

We also used SIC estimates from ice charts generated from various sensors by the National Ice Center (Fetterer and Fowler, 2009) to identify regions of interests to compute the 100% ice-tie-points.

3   Theoretical model of sea ice radiation at microwave wavelengths

Passive radiometers measure brightness temperature T_B at antenna frame with different incidence angle. T_B can be expressed
25   as:

$$T_B = \Upsilon \left[T_{B_{SURF}} + T_{B_{ATM\_DN}} \right] + T_{B_{ATM\_UP}}, \tag{1}$$

where Υ is the atmosphere transmitivity, $T_{B_{SURF}}$ the radiation emitted by the surface, $T_{B_{ATM\_DN}}$ the downward-emitted atmospheric radiation that gets scattered by the terrain in the direction of the antenna, and $T_{B_{ATM\_UP}}$ the upward-emitted atmospheric radiation.
30   The surface emission is defined as:

$$T_{B_{SURF}}(\theta) = e_s(\theta)T, \tag{2}$$

where θ is the incidence angle relative to zenith angle, e_s the surface emissivity, and T the physical temperature of the radiation-emitting body layer. Hereafter, we will use T_B to refer to surface brightness temperature, for simplicity.

The emissivity e and reflectivity Γ of a layer are related by $e = (1 - \Gamma)$. The reflectivity (sometimes also called R) is the ratio between reflected and incident radiation at the media boundaries for each polarization. Γ for horizontal H and vertical V polarizations can be calculated using Fresnel equations, which depend non-linearly on the dielectric constant (ε), and on the incident θ_i and refracted θ_t angles:

$$\Gamma_H(\theta) = \left| \frac{\sqrt{\varepsilon_1}\cos\theta_i - \sqrt{\varepsilon_2}\cos\theta_t}{\sqrt{\varepsilon_1}\cos\theta_i + \sqrt{\varepsilon_2}\cos\theta_t} \right|^2, \qquad \Gamma_V(\theta) = \left| \frac{\sqrt{\varepsilon_2}\cos\theta_i - \sqrt{\varepsilon_1}\cos\theta_t}{\sqrt{\varepsilon_1}\cos\theta_t + \sqrt{\varepsilon_2}\cos\theta_i} \right|^2. \tag{3}$$

The frequency-dependent dielectric constant of a medium is a complex number defined as $\varepsilon(f) = \varepsilon'(f) + i\varepsilon''(f)$, where the real part ε' is related to the electromagnetic energy that can be stored in the medium, and the imaginary part ε'' is related to the energy dissipated within the medium, and f is frequency. Note that brightness temperature varies linearly with emissivity (Eq. 2), hence also with reflectivity.

To calculate the brightness temperature T_B of sea ice, we will assume a sea ice model consisting of horizontal layers of three media – air, snow, and thick ice. We use the incoherent approach (i.e., conservation of energy, instead of wave field treatment in the coherent approach). Then a plane-parallel radiative transfer model (Eq. 4) is used to propagate to the surface the reflectivity computed at and through the ice-snow and snow-air media boundaries, and making a number of simplifying assumptions. Specifically, our model assumes (a) that the media are isothermal and (b) that the thickness of the ice layer is semi-infinite so that radiation from an underlying fourth layer (i.e., seawater) does not need to be considered. This approach is similar to that used by other authors (e.g., Mills and Heygster, 2011b; Maaß, 2013; Schwank et al., 2015). These assumptions are realistic for the emission of sea ice that is thicker than about 60 cm at the observing frequency of SMOS, as discussed in Section 1, since the underlying seawater then makes no contribution to the overall emissivity.

To further simplify our approach, we assume that the snow layer in the model consists of dry snow, which is typical of winter Arctic conditions. Dry snow can be considered a lossless medium at 1.4 GHz, due to the fact that the imagenary part of ε is very small compared with the real part, as stated in Schwank et al. (2015). That means that there is no attenuation in the snow layer, and therefore its attenuation coefficient, α_{snow}, is considered zero. We make this simplifying assumption because water in a wet snow layer would cause attenuation and therefore increase the total emissivity, but it is rarely possible to obtain meaningful data on the amount of water in wet snow. However, dry snow still has an effect on the refracted angle according to Snell's law, hence on the emissivity, which is computed via Eq. (3). The permittivity of dry snow depends on snow density (Tiuri et al., 1984; Matzler, 1996), which depend on the snow temperature. For a snow density of $\rho_s = 300\,g/cm^3$, the dry snow permittivity at L-band is $\varepsilon_{snow} = 1.53$ following the equation described in Schwank et al. (2015).

We can now define the simplified brightness temperature that results from an infinite number of reflections between the three medias as (Ulaby et al., 1986):

$$T_B(\theta, p, f) = \left(\frac{1 - \Gamma_{as}}{1 - \Gamma_{as}\Gamma_{si}\exp^{-2\tau}} \right)$$
$$\cdot \left[(1 + \Gamma_{si}\exp^{-\tau})(1 - \exp^{-\tau})T_{snow} + (1 - \Gamma_{si})\exp^{-\tau}T_{ice} \right] + T_{sky}\Gamma_{as}, \tag{4}$$

where Γ_{as} and Γ_{si} are the reflectivity at the air-snow and snow-ice boundaries, respectively, and T_{snow} and T_{ice} are the physical temperature in the snow and ice layers, respectively. The term τ is the attenuation factor and is defined as $\tau = 2 d \alpha \sec \theta$, where d is the depth of the snow layer and α the attenuation constant. T_{sky} is the temperature of the cosmic background. The dependence of T_B on θ, p, and f is embedded in the expressions of Γ and τ.

5   The attenuation constant α of the middle layer, in the case of a low-loss medium ($\varepsilon^{''}/\varepsilon^{'} << 1$), can be expressed as:

$$\alpha = \frac{\pi f}{c} \frac{\varepsilon^{''}}{\sqrt{\varepsilon^{'}}} \tag{5}$$

where c the speed of light. The skin depth is defined as $\delta_s = 1/\alpha$ (m) and characterizes how deep an electromagnetic wave can penetrate into a medium (e.g. Ulaby and Long, 2014).

To compute the complex dielectric constant of sea ice ε_{ice}, which is needed to compute Γ_{si}, we use the classic empirical

10   relationship by Vant et al. (1978). In this model, permittivity depends linearly on the ice brine volume V_b as,

$$\hat{\varepsilon}_{ice} = a_1 + a_2 V_{br} + i(a_3 + a_4 V_{br}) \tag{6}$$

where $V_{br} = 10 V_b$, and the coefficients a_i can be obtained by linear interpolation to 1.4 GHz of the laboratory values from microwave measurements at 1 and 2 GHz (refer to Vant et al. (1978) for coefficient values).

The sea ice brine volume V_b can be computed using Cox and Weeks (1983) as follows:

$$15 \quad V_b = \frac{\rho S}{F_1(T) - \rho S F_2(T)} \tag{7}$$

where ρ, S, and T are sea ice density, salinity, and temperature, respectively. The F functions are cubic polynomials derived empirically, namely

$$F_j(T) = \sum_{i=0}^{3} a_{ij} T^i \tag{8}$$

where the values of the coefficient a_{ij} were given in Leppäranta and Manninen (1998) for ice temperatures between –2 °C and

20   0 °C, and for lower temperatures in Cox and Weeks (1983); see also Thomas and Dieckmann (2003).

Figure 2 shows the dependence of brightness temperature, at L-band, with angle of incidence for seawater and sea ice, as well as that of ice overlaid by a dry snow layer (following Eq. 4), for nominal Arctic temperature and salinity values. Specifically, temperature and salinity values used were after Maaß (2013); for seawater –1.8°C and 30 g/Kg, respectively, and for sea ice –10°C and 8 g/Kg. Note that the T_B of seawater is significantly less than that of ice, and that the latter is slightly less than that

25   of snow over ice. Also note the non-linear dependence of T_B on incidence angle, the difference between H- and V-polarized waves for all three cases, and the larger variation with incidence angle of H than V over ice and snow (e.g., Maaß et al., 2015).

We also calculate the theoretical emissivity e_s of a four-layer model using the Burke et al. (1979) equation. The additional layer in this model is the seawater under sea ice, and we use the dielectric constant of seawater from Klein and Swift (1977). This layer does not need to be considered for the case of (optically) thick ice, but it becomes "visible" for the case of (optically)

30   thin ice (i.e., thicknesses ≤60 cm, depending on ice temperature and salinity). The expression of T_B for a four-layer model is

defined in Burke et al. (1979) as:

$$T_B(\theta, p) = \sum_{i=1}^{3} T_i \cdot \left(1 - e^{(-\gamma_i(\theta)\Delta z_i)}\right) \cdot \left(1 + \Gamma_{p,i+1}(\theta)e^{(-\gamma_i(\theta)\Delta z_i)}\right) \cdot$$

$$\prod_{j=1}^{i} [1 - \Gamma_{p,i+1}(\theta)] \cdot e^{\left(-\sum_{j=2}^{i} \gamma_{j-1}(\theta)\Delta z_{j-1}\right)} \tag{9}$$

where T_i is the temperature of each layer, Γ its reflectivity, γ the absorption coefficient, and Δz the layer thickness. The net effect of reducing the sea ice thickness and starting to sense seawater, is a decrease in surface emissivity, hence of T_B (as illustrated in Figure 5), relative to emissivity of thick ice (Shokr and Sinha, 2015).

4 Methods

4.1 Definition of robust indices from brightness temperature

It is rarely possible to obtain the ancillary geophysical data such as sea ice temperature, salinity, and ice thickness that is required to estimate brightness temperature from a microwave emission model. Therefore, making assumptions and approximations becomes critically important. It is possible, however, to define a number of indices resulting from a combination of brightness temperature observations that are less sensitive to the unknown physical parameters. For example, estimates of soil moisture or sea ice concentration from radiometric measurements are often derived by combining T_B measurements obtained from different polarizations, frequencies, and angles of incidence (Becker and Choudhury, 1988; Owe et al., 2001).

Hereafter, we use two indices, the polarization difference (PD) index and the angular difference (AD) index. The PD index is defined as the difference between T_B measurements obtained at vertical T_{B_V} and horizontal T_{B_H} polarizations as

$$\text{PD}(\theta) = T_{B_V}(\theta) - T_{B_H}(\theta). \tag{10}$$

The AD index is defined as the difference between two vertical polarization T_B measurements obtained at two different angles of incidence as

$$\text{AD}(\theta) = T_{B_V}(\theta + \Delta\theta) - T_{B_V}(\theta). \tag{11}$$

Figures 3 and 4 show the variation of PD and AD for the thick-ice model with angle of incidence, respectively. In defining AD, we use vertical rather than horizontal polarization because identification of the three media is facilitated by the larger dynamic range and non-crossing signatures of vertical polarization (Figure 4). We choose $\Delta\theta = 35°$ angle difference because this value represents a good compromise between sensitivity of the index and radiometric accuracy in the case of SMOS (Camps et al., 2005) and, importantly, is also well supported by the wide range of satellite viewing angles that characterizes SMOS.

Although the Polarization Ratio (PR) is also a commonly used index, we have chosen PD after verifying that its dynamic range is larger than that of PR, and suspecting that PD would yield higher accuracy estimates given the SMOS error budget.

4.2 Calibration of sea ice concentration using tie-points

Tie-points are widely used for retrieving SIC with higher frequency radiometers, as well as in other fields such as photogrammetry (e.g., Khoshelham, 2009). In this study, we use tie-points as the typical T_B values for 100% and 0% concentrations which permit us to compute the sea ice concentration. Tie-points can therefore be viewed as SIC calibration points because their expected radiation can be unambiguously determined.

Figure 3 shows theoretical PD tie-point values for open water and sea ice, as well as ice with a snow layer. The values for an angle of incidence of 50° are marked by solid red circles. This angle represents a good compromise in PD contrast between the two media and SMOS accuracy (Camps et al., 2005). The two bounding values are 62.9 K for seawater and 26.8 K for ice with snow cover (Table 1). The large difference between tie-point values suggests that it is possible to estimate SIC at L-band.

Figure 4 shows theoretical AD tie-point values for difference in incidence angle $\Delta\theta = 35°$ and angles of incidence up to $\theta = 30°$ which, per Eq. 11, represents the T_{B_V} difference between $\theta = 60°$ and $\theta = 25°$. The values for an angle of incidence of 25° are marked by solid red circles, for which the tie-points are 51.8 K for seawater and 8.6 K for ice with snow cover (Table 1). Hereafter, PD and AD are evaluated at the incidence angles of $\theta = 50°$ and $\theta = 25°$, respectively.

Figure 5 shows that T_B at nadir increases non-linearly as function of ice thickness up to the saturation value of $\sim$250 K, which is reached when ice becomes about 70-cm thick. Notice that T_B estimates start at an ice thickness of 5 cm because there is a discontinuity in the Burke model as the thickness of ice tends to zero (e.g., Kaleschke et al., 2010; Mills and Heygster, 2011a; Maaß, 2013; Kaleschke et al., 2013). Compared with T_B, the total variation of both AD and PD with ice thickness is significantly smaller and, therefore, are better suited to estimate sea ice concentration.

4.3 Sensitivity of estimates of sea ice concentration to surface emissivity changes

In this section, we calculate the sensitivity of SIC estimates to changes in surface emissivity due to variations in the physical properties of sea ice (i.e., salinity, temperature, and thickness). We work with estimated SIC derived from the three indices T_B, PD, and AD. This is done following a standard error propagation method (as also used in Comiso et al. (1997)). It is important to determine how changes in ice conditions affect SIC estimates through those three indices to try to minimize SIC errors obtained using SMOS.

Table 2 lists the sensitivities, according to our theoretical model, of the indices I ($I = T_B$, PD, and AD) to the geophysical variables of ice and seawater: physical temperature (i.e., $\delta I/\delta T$), salinity ($\delta I/\delta S$), and thickness ($\delta I/\delta d$) evaluated within the ranges of T_{water}=[2,15], S_{water}=[10,38], T_{ice}=[-20,-5], and S_{ice}=[2,12]. It should be noted that those sensitivities are calculated using the model and the nominal Arctic temperature and salinity values defined in Section 3. In order to assess which index is less sensitive to changes in a given geophysical variable, we calculate absolute sensitivities, defined as the sensitivities multiplied by the dynamic range of the measurements.

Knowing the value of the tie-points of sea ice (SIC=100%) and seawater (SIC=0%), one can compute the average slopes of the SIC estimates to their corresponding parameters T_B, PD, and AD (i.e., $\delta SIC/\delta T_B$, $\delta SIC/\delta PD$, and $\delta SIC/\delta AD$). From

data in Table 1, we obtain the average slopes as: $\delta SIC/\delta T_B = 0.65$, $\delta SIC/\delta PD = 2.32$, and $\delta SIC/\delta AD = 2.77$. These slopes can be used to propagate T_B, AD, and PD errors to errors in the SIC estimates.

We assume reasonable values for the variability of the physical parameters on which our emissivity model depends on, namely T, S and d of ice (generically denoted by g), as follows: ΔT=5 K, ΔS=4 g/Kg, and Δd=30 cm. Using the values in Table 2 and the calculated average slopes, one can finally compute the errors in SIC estimates associated with the geophysical variability of g when the index I is used to evaluate SIC as:

$$\Delta SIC|_g = \left| \frac{\delta SIC}{\delta I} \right| \cdot \left| \frac{\delta I}{\delta g} \right| \cdot \Delta g \tag{12}$$

To evaluate the final impact of geophysical variability on the SIC evaluation using the index I, we compute the root-sum-squared (RSS) of the SIC uncertainties due to the geophysical parameters (Table 3). The table shows that AD is the most robust index to retrieve SIC, slightly better than PD, and significantly better than T_B. Because T_B is theoretically more sensitive to thin ice than the other two indices, one can expect that the use of T_B to retrieve SIC would result in larger SIC errors. Moreover, the uncertainty distribution of T_B is too broad, especially due to thickness, thus less adequate to fulfill the statistical hypotheses used to derive SIC. Despite the uncertainties in the theoretical physical model of ice, we consider the differences significant enough to focus on inversion algorithms using the PD and AD indices, and not on T_B.

4.4 Comparison with empirical tie-points

Following the theoretical analysis, we now turn to evaluate its performance empirically. We therefore select several regions of interest in the Arctic Ocean where SIC has been determined to be either 0% or 100% by other sensors and methods. To identify such regions, we use SIC maps from OSI-SAF and from the National Ice Center. In particular, we selected the open seawater region between latitudes 55°–70° N and longitudes 20° W and 25° E, which comprises more than 2000 pixels in a typical SMOS image. For sea ice, we selected the multi-year (MY) ice region between latitudes 78°–83° N (the northernmost latitude observable by SMOS) and longitudes 75°–150° W, which comprises about 1000 pixels per SMOS image. We expect some level of uncertainty associated with the selection of the region to compute the 100% tie-points for summer periods stemming from known errors in the summer SIC products by OSI-SAF (Tonboe et al., 2016).

We calculated SMOS brightness temperatures of these target regions to evaluate their potential as empirical tie-points for seawater and sea ice. The temporal variation, in 2014, of the spatially averaged (median) T_B at nadir of the two geographic regions are shown in Figure 6. The values are consistent with the modeled values in Table 1. For the seawater region, the figure shows that the brightness temperature is constant, at about 99 K, to within $\sim$2.5 K (one σ standard deviation) throughout the year. For the ice region, T_B is also stable during the non-summer months, but it drops by about 20 K during the summer season due to changes in surface emissivity associated with snow and ice melt and concurrent formation of meltwater ponds. The factor-two increase in formal error in summer relative to winter is also an indication of increased radiometric variability in surface conditions (as shown in Table 1).

Figure 7 shows that the temporal radiometric stability of the seawater region during 2014, and that of sea ice during the non-summer months, is also reflected in the AD and PD indices, as one would expect. This suggests that a different set of

tie-points during winter and summer periods could be beneficial for the quality of the SIC retrievals. On the other hand, the AD and PD tie-point values are very stable during winter and spring (November to June), indicating that values are robust to variations on physical temperature and that may not be necessary to compute tie-point values often (daily or monthly), as done with the OSI-SAF product.

5   Figure 8 shows a 2-D scatter plot of AD and PD indices for the two regions defined above during March (winter tie-point) and July (summer tie-point) 2014. The index values associated with seawater and with ice group form two well-differentiated clusters, which implies that the two types of regions can be clearly segregated using these indices. This is also true for the summer tie-points even though in this case the dispersion is larger and values are closer to sea tie-points, as expected following Figure 7.

10   The modeled (with snow and without) and observed TB, AD, and PD tie-point values for winter and summer 2014, and the standard deviation (σ) of the measurements are listed in Table 1. It is encouraging that most of the values are in agreement at about 2σ despite underlying model assumptions such as uniform sea ice temperature and specular ocean surface. Another important result is that the observed SMOS data is closer to the model when snow is considered.

4.5   Retrieval of sea ice concentration

15   The brightness temperature of mixed pixels, that is, ocean pixels partially covered by sea ice, can be expressed as a linear combination of the brightness temperature of ice and seawater weighted by the percentage of each surface type (e.g., Comiso et al., 1997):

$$T_{B_{mixed}} = C\,T_{B_{ice}} + (1 - C)\,T_{B_{water}} \tag{13}$$

where C is the fraction of ice present in a pixel, with $C = 1$ corresponds to 100% of ice and $C = 0$ to 0% of ice, or equivalently
20   100% of seawater. Since AD and PD (Eqs. 10-11) depend linearly on brightness temperature, Eq. (13) can be used to express both AD and PD.

There are several possible strategies to estimate sea ice concentration at a given pixel from the AD and PD values measured at that pixel. The simplest approach is to consider that the values of the tie-points are good representatives of the values of AD and PD at the respective medium, i.e., seawater and sea ice, such that

25   $$\mathrm{AD} \approx C\,\mathrm{AD}_{ice} + (1 - C)\,\mathrm{AD}_{water}$$

$$\mathrm{PD} \approx C\,\mathrm{PD}_{ice} + (1 - C)\,\mathrm{PD}_{water} \tag{14}$$

Concentration C can thus be retrieved from the value of either AD or PD by inverting the associated linear equation. In general, C can also be evaluated simultaneously with the AD and the PD observations by averaging the values obtained from both indices, as:

30   $$C = \frac{1}{2}\left[\frac{\mathrm{AD} - \mathrm{AD}_{water}}{\mathrm{AD}_{ice} - \mathrm{AD}_{water}} + \frac{\mathrm{PD} - \mathrm{PD}_{water}}{\mathrm{PD}_{ice} - \mathrm{PD}_{water}}\right] \tag{15}$$

This is known as the Linear Estimation of SIC. However, this approach might be too simple, as the values of AD and PD on ice and seawater can have some non-negligible dispersion due to geophysical conditions and to radiometric noise.

In this paper, a new inversion algorithm to estimate C is presented, which considers that AD and PD have known distributions, and by combining the observations it is possible to infer the value of C that is statistically more probable.

5   The distributions of the SMOS AD and PD are unimodal and symmetric (not shown), thus allowing us to approximate them by Gaussians and considering the pure ice and pure sea measurements as independent. Therefore we can easily use a Maximum-Likelihood Estimation (MLE) approach. The MLE has many optimal properties in statistical inference such as (e.g., Myung, 2003) sufficiency (the complete information about the parameter of interest is contained in the MLE estimator), consistency (the true value of the parameter that generated the data is recovered asymptotically, i.e. for sufficiently large samples), efficiency

10 (asymptotically, it has the lowest-possible variance among all possible parameter estimates), and parameterization invariance (same MLE solution obtained independent of the parametrization used).

Assuming the linearity superposition of indices (Eq. 14), it follows that the distributions of AD and PD (f_{AD}, f_{PD}) in a general ocean pixel can be expressed as:

$$f_{\text{AD}} \sim \mathcal{N} \left(C\,\overline{\text{AD}}_{ice} + (1-C)\,\overline{\text{AD}}_{water}, \sqrt{C^2\,\sigma^2_{\text{AD}_{ice}} + (1-C)^2\,\sigma^2_{\text{AD}_{water}}} \right) \tag{16}$$

$$f_{\text{PD}} \sim \mathcal{N} \left(C\,\overline{\text{PD}}_{ice} + (1-C)\,\overline{\text{PD}}_{water}, \sqrt{C^2\,\sigma^2_{\text{PD}_{ice}} + (1-C)^2\,\sigma^2_{\text{PD}_{water}}} \right) \tag{17}$$

where the bar over the AD and PD indices refers to their mean values, the subindex identifies the medium, and σ is the associated standard deviation for each index and media. To obtain the mean and standard deviation values, we used the SMOS measurements at the regions for generating tie-points and periods discussed in Sect. 4.4. The symbol $\mathcal{N}$ means normal probability density function.

20 As a first approximation, we have considered AD and PD two independent variables. It thus follows that the likelihood function $\mathcal{L}$ is equal to the product of their distributions or, equivalently and conveniently, to their sum (recall that the likelihood is the logarithm of the probability density function), thus:

$$\widehat{l} = \ln(\mathcal{L}) = \ln(f_{AD}) + \ln(f_{PD}) \tag{18}$$

The MLE of SIC is the value of C that maximizes the likelihood function $\widehat{l}$.

25 ## 5   Results

5.1   Quality algorithm assessment

We have calculated AD and PD values from SMOS brightness temperature and used the MLE approach to obtain SIC estimates over the Arctic Ocean in year 2014. We have estimated SIC using different tie-points, characterized by their central value and

dispersion. For seawater, we have used a single, year-round median value and the associated standard deviation for each index. For ice tie-points, we have used two sets of values, as suggested by the results in Figure 7. For the first set, we have computed for all years the median of the tie-points between December and May (Table 1), i.e., the winter-spring months when Arctic sea ice extent is close to its annual maximum. For the second set, we have used those same winter-spring values for the months of October through May but the average of the summer values for the months between June and September (Table 1). We have not used the October nor November data to compute ice tie-points values because these are months of maximum extension of thin ice, and underlying emission through thin ice could cause some errors on the SIC estimates (Figure 5 and Table 2).

The root-mean-square (RMS) error of SIC retrievals relative to OSI-SAF over the Arctic Ocean is shown in Figure 9. Four types of retrievals and two sets of tie-points are compared. Introducing a specific set of summer tie-points (black solid line) reduces the RMS error with respect to using only one unique tie-point for the whole year (black dotted line). The RMS reduction is about 24% and 12% in July and August, respectively, and to smaller degree in June and September. Therefore, we will hereafter use a different set of tie-points values in summer and winter.

Furthermore, using the set of summer-winter tie-points, results from four types of inversions that stem from combinations of linear and MLE method and indices are compared in Figure 9. The lowest RMS values through all months in 2014 but January are obtained with the MLE inversion algorithm and the AD index alone. The evolution along the year of the RMS obtained with the linear retrieval method is similar in the case of the MLE method, but at ∼5-10% increased noise level. Larger RMS values and increased temporal variability are observed when the PD index is also used. The RMS error of all retrievals is largest in Fall, in particular if the PD index is used. Those are months of ice formation, therefore vast regions become covered with frazil ice, nilas, and thin young ice, following the minimum ice extension of September. All methods converge to similar results in September, since this period is the one with minimum ice extension and minimum thin ice is expected (so resulting in very small difference between using AD or AD and PD methods).

The spatial variation of the difference in MLE SIC retrievals when using only the AD index and when using the AD and PD indices for the period 2–5 November 2014 is shown in Figure 10. As expected, the largest differences are associated with regions of thin ice formation, in particular in the Laptev Sea, Kara Sea, and along the edge of the ice pack both in the western Arctic and the Atlantic sector. Together, the spatio-temporal snapshots in Figures 9-10 highlight the sensitivity of PD to the presence of thin ice, what naturally leads to an increase of the retrieval error when PD is used. This conclusion is not fully consistent with the analysis done using the models in Section 4.3, on the dependence of the indices (T_B, PD, AD) on ice thickness. Table 2 shows that, theoretically, PD is slightly less sensitive to thin ice than AD. However, the AD index is the least sensitive (lowest RSS) to variations of all the analyzed variables. Therefore, we will hereafter use the AD index, summer-winter tie-points values, and an MLE-based estimator for SIC retrievals.

5.2 Accuracy assessment of SMOS SIC retrievals

We have evaluated the mutual consistency of the SMOS SIC retrievals, and in the process we have determined which is the approach that leads to the minimum error in the retrieval of SIC. We now evaluate the accuracy of those retrievals. Although a representative (in the space-time domain) ground-truth dataset that allows us to assess the accuracy of SMOS retrievals does

not exist, the SIC estimates from OSI-SAF are a good option for cross-check. They are independent from SMOS, the spatio-temporal sampling and resolution of their products is commensurate with that of SMOS, and their error budget is available.

The spatial distribution of SMOS SIC in the Arctic Ocean has been estimated from SMOS data for the 3-day period 2–5 March 2014 and it has been compared with OSI-SAF SIC product on 4 March 2014 . The largest differences between both algorithms are located at the margins of the sea ice cover, where thinner ice can be expected (see Figure 11). March is the month of maximum sea ice extent, but the results for other winter months are similar.

On the other hand, November is the month of maximum extension of thin young ice, specially through the Beaufort Sea since ice in the Laptev and Kara seas remains thin during winter (Shokr and Dabboor, 2013). Significantly larger differences between SMOS and OSI-SAF products are now observed over a much wider area of the Arctic Ocean including the Barents, Kara, Laptev, East Siberian, and Beaufort seas (Figure 12).

The brightness temperature measured by a passive microwave radiometer, increases with sea ice thickness up to a saturation value. Such an increase is more gradual for low frequencies and horizontal polarization (e.g., Ivanova et al., 2015). At the SMOS L-band, the increase of emissivity with ice thickness reaches saturation for an ice thickness that is about 60 cm, depending on ice salinity and temperature (Kaleschke et al., 2012) whereas at the OSI-SAF frequencies (19 and 37 GHz) is only a few cm (Heygster et al., 2014; Ivanova et al., 2015). For example, for pixels that are 100% covered by thin ice of say 25-cm thickness, the AD and PD values for those pixels will be slightly different than the tie-point value of ice because the value of ice tie-points was computed from thick, MY ice (see Figure 5) for model analysis. This contrast leads to a difference in classification of such pixels, that will be considered mixtures of water and ice in the case of SMOS, and as 100% ice with OSI-SAF. In other words, the estimation of SIC of a seas covered by frazil ice and nilas will be higher for OSI-SAF than for SMOS.

To further analyze this classification difference, we have calculated the probabilities of SMOS SIC conditioned by values of OSI-SAF SIC using a full year, 2014, of Arctic-wide estimates. The probability of estimating a SIC value with SMOS that is less or equal than 5% when the estimated OSI-SAF SIC is 0% is shown in Figure 13 (red line). As expected, the conditioned probability is very high throughout the year. This implies that both products have a similar ability to detect (close to) 100% ocean pixels. This implies that the probability of having high SMOS SIC values when OSI-SAF is low, is almost zero, which also means that the rate of triggering false alarms on ice detection with SMOS is low.

On the contrary, the probability of estimating a SMOS SIC equal or higher than 90% while the OSI-SAF SIC is 100% is not constant during the year and decrease with respect to the previous case. During the winter period (between January and April), the conditioned probability is notably high (near 0.9) (see Figure 13 blue line). Then it decreases sharply during spring and most notably in summer. This change in the conditioned probability starting in the spring could stem from a change in ice properties. As the snow becomes wetter with the onset of the melt season the observed emissivity starts to change, and this, varies with the observating frequency (different scattering response). The observed increase of the conditioned probability in June could be due to the use of a summer tie-point (applied from June to September) which improve the RMS with respect to OSISAF as shown in Figure 9. The low conditioned probability in Fall can be explained by the presence of thin ice.

We have analysed the spatial distribution of the conditioned probability of SIC estimates for the months of March and November. Those regions where OSI-SAF SIC is more than 0.9 while SMOS SIC is less than 0.9 (light blue color in Figures 14)

outline the edge of the ice cover. This is in good correspondence with the expected areas of thin ice. Besides, this condition is extended when analysing November data (Figure 14b) when thin ice is more frequent in the Arctic.

During the winter months, the spatial coefficients of determination (r^2) between SMOS and OSI-SAF SIC is high (more than 0.65), what again is consistent with our interpretation about the role of thin ice in SMOS SIC (see Figure 15). As melt starts, the correlation between SIC estimates continues to be high, thanks to the use of the summer tie-point in the retrieval. In September, ice cover extent is at minimum because ice growth has not started yet there is almost no thin ice, and the correlation remains high. The correlation drops in the Fall (between October and December) because ice growth starts by freezing of the sea surface, producing large amounts of new thin ice. To compute these values, we have only included SIC values between 0.05 (5%) and 0.95 (95%) when computing correlations to avoid the two extremes values leading to too high, non-significant values of correlation.

6   Discussion

The two PD and AD indices, which are derived from brightness temperature, have been designed to maximize their differences between open water and sea ice. Both have a low response to changes in the geophysical characteristics of the media, which has been confirmed by using theoretical models and by performing sensitivity analysis.

The tie-points, defined as the characteristic values of our reference indices on the different media, have been calculated from SMOS data. When compared to theoretical values, some small discrepancies at the 10-20% level have been observed, probably due to simplifying assumptions such flat surface ice, flat sea, and constant temperature at the layers used in the theoretical models. We have thus decided to follow a more empirical approach. The use of two sets of tie-points, one for summer and one for winter measurements, improves the results of the summer SIC maps relative to a static unique tie-points. This improvement is not caused by changes in the ice or sea physical temperature, but most probably changes in the ice properties, because as snow and ice become wetter during the melt season, the observed radiometric emission changes. This effect is also observed on measurements from radiometers at higher frequencies than SMOS.

We have introduced the MLE inversion algorithm to retrieve SIC from SMOS data. The method is based on the maximization of the a posteriori likelihood of the joint distribution of AD and PD indices, assuming that they are independent and normally distributed. This MLE algorithm is more robust (less noisy) than the linear inversion (Eq. 14). It also improves the retrieved SMOS SIC with respect to a linear inversion method because the former takes into account the dispersion (error) of the tie-points (reference), which makes the algorithm more robust to T_B errors. SIC maps obtained using only the AD index are of better quality than when the AD and PD indices are used together. We attribute this to the higher sensitivity of PD than AD to physical changes in the media.

SMOS and OSI-SAF SIC maps compare well in terms of correlation (determination coefficient higher than 0.65) and RMS except in areas of thin sea ice. This difference can be explained by the higher penetration of SMOS in sea ice (about 60 cm) relative to the penetration from higher frequency radiometers. Thus, when ice is thinner than 60 cm SMOS data lead to lower values of SIC that OSI-SAF.

7 Conclusions

Estimating SIC using L-band observations such as those from SMOS is recommended for the negligible effect of the atmosphere on brightness temperatures, and also because the vertical polarization of T_B is insensitive to snow depth (Maaß et al., 2015).

Two indices derived from brightness temperature, PD and AD, have been chosen, since they verify the two required conditions: they maximize the difference between open water and sea ice, and they present a low response to changes in the geophysical characteristics of the media. AD and PD tie-point values have been shown to be very stable during winter and spring periods (Figure 7), indicating that the values are robust to variations in physical temperature. Thanks to that, one can safely assume two sets of static (i.e., not temporally varying) tie-points, one for summer and and one for winter for SMOS data, and not fortnightly or monthly as is done in case of the OSI-SAF product.

We have shown that the best configuration for SIC retrieval is using AD only with the MLE inversion method. We exclude PD and T_B because they are more sensitive to ice thickness; therefore, the combined use of AD and PD presents larger errors when thin ice is present (fall). The MLE inversion method presents better results than a linear inversion since it takes into account the uncertainty of the tie-points.

SIC estimates from SMOS have some drawbacks with respect to those from higher-frequency radiometers. For example, whereas the spatial resolution of the high-frequency SIC estimates can reach ∼3 km, the resolution from SMOS will not be better than about 35 km. A second issue of SMOS is that it underestimates SIC in the presence of thin ice, which is characteristic of the ice edges and freeze-up periods. Therefore, SMOS data should be used in combination with some form of spatial masking for those regions. We suggest that SIC estimates from SMOS can complement those from higher-frequency radiometers, together yielding enhanced SIC products.

This dataset could be very beneficial during summer period, since SMOS SIC, theoretically, should be less sensitive to summer metamorphosis, due to the larger wavelength. Previous works show that the T_B and SIC measured at 6.9 GHz band are more robust to summer ice changes than higer frequency measurements (Kern et al., 2016; Gabarro, 2017). The confirmation of this statement will be done as future work.

Data availability. Level 1 SMOS data can be obtained from ESA distribution system (https://earth.esa.int/web/guest/data-access). OSI SAF sea-ice concentration is provided by OSI SAF via ftp://osisaf.met.no/archive. Sea ice charts are generated by the National Ice Center (https://nsidc.org/data/g02172).

Author contributions. C. Gabarro and P. Elosegui conceived the study. C. Gabarro and J. Pla-Resina (during his master thesis) developed the study to choose the best indices using modelling simulations. P Elosegui gave advice on physics of the ice and on the datasets available for validation. A. Turiel contributed with new mathematical concepts, and M. Portabella gave support in the sensitivity analysis. C. Gabarro wrote the paper, and all co-authors contributed to the discussion and gave input for writing.

Competing interests. The authors declare that they have no conflict of interest.

Acknowledgements. This study has been funded by the National R+D Program of the Spanish Ministry of Economy through the Promises project ESP2015-67549-C3-R, as well as by previous SMOS-related grants. The authors would like to thank the referees for their valuable comments which helped to improve the manuscript and authors want to remark that this work has been possible thanks to the collaboration of the whole BEC team.

References

AMAP: Changes in Arctic Snow, Water, Ice and Permafrost, Arctic Climate Issues 2011: Arctic Monitoring and Assessment Programme (AMAP), SWIPA 2011 Overview Report, Oslo, 2012.

Becker, F. and Choudhury, B. J.: Relative Sensitivity of Normalized Difference Vegetation Index (NDVI) and Microwave Polarization Difference Index (MPDI) for Vegetation and Desertification Monitoring, Remote Sensing of Environment, 24, 297–311, https://doi.org/DOI: 10.1016/0034-4257(88)90031-4, 1988.

Brodzik, M. J. and Knowles, K. W.: EASE-Grid: A Versatile Set of Equal-Area Projections and Grids, Discrete Global Grids, 2002.

Burke, W., Schmugge, T., and Paris, J.: Comparison of 2.8- and 21-cm Microwave Radiometer Observations Over Soils With Emission Model Calculations, Journal of Geophysical Research, 84, https://doi.org/DOI: 10.1029/JC084iC01p00287, 1979.

Camps, A., Vall-llossera, M., Duffo, N., Torres, F., and Corbella, I.: Performance of Sea Surface Salinity and Soil Moisture Retrieval Algorithms with Different Ancillary Data Sets in 2D L-band Aperture Synthesis Interferometic Radiometers, IEEE Transactions on Geoscience and Remote Sensing, 43, 1189–1200, https://doi.org/10.1109/TGRS.2004.842096, 2005.

Cavalieri, D., Gloersen, P., and Campbell, W.: Determination of sea ice parameters with the NIMBUS 7 SMMR, Journal of Geophysical Research, 89, 5355–5369, https://doi.org/DOI: 10.1029/JD089iD04p05355, 1984.

Cohen, J., Screen, J. A., Furtado, J. C., Barlow, M., Whittleston, D., Coumou, D., Francis, J., Dethloff, K., Entekhabi, D., Overland, J., and Jones, J.: Recent Arctic amplification and extreme mid-latitude weather, Nature Geoscience, 7, 627–637, https://doi.org/10.1038/NGEO2234, 2014.

Comiso, J. C.: Characteristics of arctic winter sea ice from satellite multispectral microwave observations, Journal of Geophysical Research., 91, 975–994, https://doi.org/10.1029/JC091iC01p00975, 1986.

Comiso, J. C.: Large Decadal Decline of the Arctic Multiyear Ice Cover, Journal of Climate, 25, 1176–1193, https://doi.org/10.1175/JCLI-D-11-00113.1, 2012.

Comiso, J. C., Cavalieri, D. J., Parkinson, C. L., and Gloersen, P.: Passive microwave algorithms for sea ice concentration: A comparison of two techniques, Remote Sensing of Environment, 60, 357 – 384, https://doi.org/10.1016/S0034-4257(96)00220-9, 1997.

Corbella, I., Torres, F., Duffo, N., Gonzalez-Gambau, V., Pablos, M., Duran, I., and Martin-Neira, M.: MIRAS Calibration and Performance: Results From the SMOS In-Orbit Commissioning Phase, Geoscience and Remote Sensing, IEEE Transactions on, 49, 3147 –3155, https://doi.org/10.1109/TGRS.2010.2102769, 2011.

Cox, G. and Weeks, W.: Equations for Determining the Gas and Brine Volumes in Sea-Ice Samples, Journal of Glaciology, Vol. 29. No. 102, https://doi.org/10.1017/S0022143000008364, 1983.

Deimos: SMOS L1 Processor Algorithm Theoretical Baseline Definition, SO-DS-DME-L1PP-0011, Tech. rep., Deimos Engenharia, 2010.

Fetterer, F. and Fowler, C.: National Ice Center Arctic Sea Ice Charts and Climatologies in Gridded Format, Version 1, http://dx.doi.org/10.7265/N5X34VDB, 2009.

Font, J., Boutin, J., Reul, N., Spurgeon, P., Ballabrera-Poy, J., Chuprin, A., Gabarró, C., Gourrion, J., Guimbard, S., Hénocq, C., Lavender, S., Martin, N., Martínez, J., McCulloch, M., Meirold-Mautner, I., Mugerin, C., Petitcolin, F., Portabella, M., Sabia, R., Talone, M., Tenerelli, J., Turiel, A., Vergely, J., Waldteufel, P., Yin, X., Zine, S., and Delwart, S.: SMOS first data analysis for sea surface salinity determination, International Journal of Remote Sensing,, DOI:10.1080/01431161.2012.716541, 2013.

Gabarro, C.: The dynamical estimation of summer sea ice tie-points using low frequency passive microwave channels, Associated Visiting Scientist 16/03, OSISAF / EUMETSAT, 2017.

Heygster, G., Huntemann, M., Ivanova, N., Saldo, R., and Pedersen, L. T.: Response of passive microwave sea ice concentration algorithms to thin ice, in: 2014 IEEE Geoscience and Remote Sensing Symposium, pp. 3618–3621, https://doi.org/10.1109/IGARSS.2014.6947266, 2014.

Holland, M. M. and Bitz, C. M.: Polar amplification of climate change in coupled models, Climate Dynamics, 21, 221–232, https://doi.org/10.1007/s00382-003-0332-6, http://dx.doi.org/10.1007/s00382-003-0332-6, 2003.

Huntemann, M., Heygster, G., Kaleschke, L., Krumpen, T., Mäkynen, M., and Drusch, M.: Empirical sea ice thickness retrieval during the freeze up period from SMOS high incident angle observations, The Cryosphere, 8, 439–451, https://doi.org/10.5194/tc-8-439-2014, 2014.

IPCC: Climate Change 2013: The Physical Science Basis, Fifth Assessement, Tech. rep., Cambridge University Press, 2013.

Ivanova, N., Pedersen, L. T., Tonboe, R. T., Kern, S., Heygster, G., Lavergne, T., Sørensen, A., Saldo, R., Dybkjær, G., Brucker, L., and Shokr, M.: Satellite passive microwave measurements of sea ice concentration: an optimal algorithm and challengesdoi:10.5194/tcd-9-1269-2015, The Cryosphere., 9, 1797–1817, https://doi.org/10.5194/tc-9-1797-2015, 2015.

Kaleschke, L., Lupkes, C., Vihma, T., Haarpaintner, J., Bochert, A., Hartmann, J., and Heygster, G.: SSM/I Sea ice remote sensing for mesoscale ocean–atmosphere interaction analysis, Canadian Journal of Remote Sensing, 27, 5, 526–537, https://doi.org/10.1080/07038992.2001.10854892, 2001.

Kaleschke, L., Maaß, N., Haas, C., Hendricks, S., Heygster, G., and Tonboe, R. T.: A sea-ice thickness retrieval model for 1.4 GHz radiometry and application to airborne measurements over low salinity sea-ice, The Cryosphere, 4, 583–592, https://doi.org/10.5194/tc-4-583-2010, 2010.

Kaleschke, L., Tian-Kunze, X., Maaß, N., Mäkynen, M., and Drusch, M.: Sea ice thickness retrieval from SMOS brightness temperatures during the Arctic freeze-up period, Geophysical Research Letters, https://doi.org/10.1029/2012GL050916, 2012.

Kaleschke, L., Tian-Kunze, X., Maaß, N., Heygster, G., Huntemann, M., Wang, H., Hendricks, S., and Krumpen, T.: SMOS Sea Ice Retrieval Study (SMOSIce). Final Report, Tech. rep., ESA ESTEC Contract No.: 4000101476/10/NL/CT., http://icdc.zmaw.de/fileadmin/user_upload/icdc_Dokumente/SMOSICE_FinalReport_2013.pdf, 2013.

Kern, S., Rösel, A., Pedersen, L. T., Ivanova, N., Saldo, R., and Tonboe, R. T.: The impact of melt ponds on summertime microwave brightness temperatures and sea-ice concentrations, The Cryosphere, 10, 2217–2239, https://doi.org/10.5194/tc-10-2217-2016, http://www.the-cryosphere.net/10/2217/2016/, 2016.

Kerr, Y., Waldteufel, P., Wigneron, J., Delwart, S., Cabot, F., Boutin, J., Escorihuela, M., Font, J., Reul, N., Gruhier, C., Juglea, S., Drinkwater, M., Hahne, A., Martin-Neira, M., and Mecklenburg, S.: The SMOS mission: New tool for monitoring key elements of the global water cycle, Proc. IGARSS 2010, no. 5., 98, 666–687, 2010.

Khoshelham, K.: Role of Tie Points in Integrated Sensor Orientation for Photogrammetric Map Compilation, Photogrammetric Engineering and Remote Sensing, 75, 305–311, https://doi.org/10.14358/PERS.75.3.305, 2009.

Klein, L. and Swift, C.: An Improved Model for the Dielectric Constant of Sea Water at Microwave Frequencies, IEEE Transactions on Antennas and Propagation, AP-25, 104–111, https://doi.org/10.1109/JOE.1977.1145319, 1977.

Leppäranta, M. and Manninen, T.: The brine and gas contents of sea-ice with attention to low salinities and high temperatures, Internal Report 2, Tech. rep., Finnish Institute of Marine Research, 1998.

Maaß, N.: Remote Sensing of Sea Ice thickness Using SMOS data, Master's thesis, Hamburg University, 2013.

Maaß, N., Kaleschke, L., Tian-Kunze, X., and T., R.: Snow thickness retrieval from L-band brightness temperatures: a model comparison, Annals of Glaciology, 56(69), doi: 10.3189/2015AoG69A886, 2015.

Markus, T. and Cavalieri, D.: An enhancement of the NASA Team sea ice algorithm, IEEE Transactions of Geoscience and Remote Sensing, 38, 1387–1398, https://doi.org/10.1109/36.843033, 2000.

Martin-Neira, M., Ribó, S., and Martin-Polegre, A. J.: Polarimetric mode of MIRAS, IEEE Transactions on Geoscience and Remote Sensing, 40, 1755–1768, https://doi.org/10.1109/TGRS.2002.802489, 2002.

5 Matzler, C.: Microwave permittivity of dry snow, IEEE Transactions on Geoscience and Remote Sensing, 34, 573–581, https://doi.org/10.1109/36.485133, 1996.

Mecklenburg, S., Wright, N., Bouzina, C., and Delwart, S.: Getting down to business - SMOS operations and products., ESA Bulletin, 137, 25–30, 2009.

Mills, P. and Heygster, G.: Retrieving Ice Concentration From SMOS, Geoscience and Remote Sensing Letters, IEEE, 8, 283–287,
10   https://doi.org/10.1109/LGRS.2010.2064157, 2011a.

Mills, P. and Heygster, G.: Sea Ice Emissivity Modeling at L-Band and Application to 2007 Pol-Ice Campaign Field Data, IEEE Transactions on Geoscience and Remote Sensing, 49, 612–627, https://doi.org/10.1109/TGRS.2010.2060729, 2011b.

Myung, J.: Tutorial on maximum likelihood estimation, Journal of Mathematical Psychology, 47, 90–100, https://doi.org/doi:https://doi.org/10.1016/S0022-2496(02)00028-7, 2003.

15 Owe, M., Jeu, R., and Walker, J.: A Methodology for Surface Soil Moisture and Vegetation Optical Depth Retrieval Using the Microwave Polarization Difference Index, IEEE Transactions on Geoscience and Remote Sensing, 39, No. 8, 1643–1654, https://doi.org/10.1109/36.942542, 2001.

Ramseier, R.: Sea ice validation, in: DMSP Special Sensor Microwave/Imager Calibration/Validation, 1991.

Schwank, M., Mätzler, C., Wiesmann, A., Wegmüller, U., Pulliainen, J., Lemmetyinen, J., Rautiainen, K., Derksen, C., Toose, P., and Drusch,
20   M.: Snow Density and Ground Permittivity Retrieved from L-Band Radiometry: A Synthetic Analysis, IEEE Journal of Selected Topics in Applied Earth Observations and Remote Sensing, 8, 3833–3845, https://doi.org/10.1109/JSTARS.2015.2422998, 2015.

SEARCH: Research, Synthesis, and Knowledge Transfer in a Changing Arctic: The Study of Environmental Arctic Change (SEARCH), Tech. rep., Arctic Research Consortium of the United States, 2013.

Shokr, M. and Dabboor, M.: Interannual Variability of Young Ice in the Arctic Estimated Between 2002 and 2009, IEEE Transactions on
25   Geoscience and Remote Sensing, 51, 3354–3370, https://doi.org/10.1109/TGRS.2012.2225432, 2013.

Shokr, M. and Sinha, N.: Sea Ice. Physics and Remote Sensing, AGU- WILEY, https://doi.org/ISBN: 978-1-119-02789-8, 2015.

Shokr, M., Lambe, A., and Agnew, T.: A new algorithm (ECICE) to estimate ice concentration from remote sensing observations: an application to 85-GHz passive microwave data, IEEE Transactions of Geoscience and Remote Sensing, 46, 4104–4121, https://doi.org/10.1109/TGRS.2008.2000624, 2008.

30 Smith, D.: Extraction of winter total sea-ice concentration in the Greenland and Barents Seas from SSM/I data, Internation Journal of Remote Sensing, 17, 2625–2646, https://doi.org/10.1080/01431169608949096, 1996.

Stroeve, J., Serreze, M., Holland, M., Kay, J., Malanik, J., and Barrett, A.: The Arctic's rapidly shrinking sea ice cover: a research synthesis, Climatic Change, 110, 1005–1027, https://doi.org/10.1007/s10584-011-0101-1, 2012.

Talone, M., Portabella, M., Martínez, J., and González-Gambau, V.: About the Optimal Grid for SMOS Level 1C and Level 2 Products, IEEE
35   Geoscience and Remote Sensing Letters, 12, 1630–1634, https://doi.org/10.1109/LGRS.2015.2416920, 2015.

Thomas, D. and Dieckmann, G., eds.: Sea Ice. An Introduction o its physics, Chemistry, Biology and geology, Blackwell, 2003.

Tiuri, M., Sihvola, A., Nyfors, E., and Hallikaiken, M.: The complex dielectric constant of snow at microwave frequencies, IEEE Journal of Oceanic Engineering, 9, 377–382, https://doi.org/10.1109/JOE.1984.1145645, 1984.
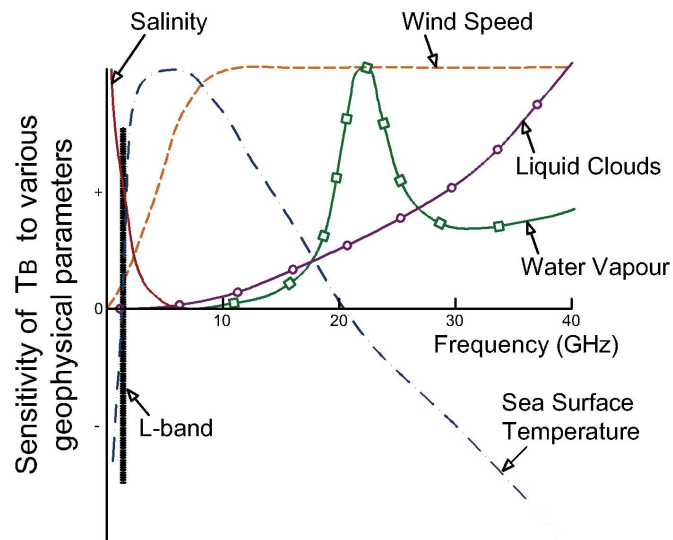
Figure 1. Sensitivity of brightness temperature for open seawater over a range of observing frequencies in the microwave band for a set of key geophysical parameters (created after Wilheit (1978) and Ulaby and Long (2014)).

Tonboe, R. T., Eastwood, S., Lavergne, T., Sørensen, A. M., Rathmann, N., Dybkjær, G., Toudal Pedersen, L., Høyer, J. L., and Kern, S.: The EUMETSAT sea ice climate record, The Cryosphere, 2016, 2275–2290, https://doi.org/10.5194/tc-10-2275-2016, 2016.

Ulaby, F. and Long, D.: Microwave Radar and Radiometric Remote Sensing., University of Michigan Press, iSBN: 978-0-472-11935-6, 2014.

5 Ulaby, F., Moore, R., and Fung, A.: Microwave Remote Sensing. Active and Passive., Addison-Wesley Publishing Company. Advanced Book Program/World Science Division., iSBN-13: 978-0890061916, 1986.

Vant, M., Ramseier, R., and Makios, V.: The complex-dielectric constant of sea ice at frequencies in the range 0.1–40 GHz, Journal of Applied Physics, 49, 1264–1280, https://doi.org/10.1063/1.325018, 1978.

Vihma, T.: Effects of Arctic Sea Ice Decline on Weather and Climate: A Review, Surveys in Geophysics, 35, 1175–1214, 10 https://doi.org/10.1007/s10712-014-9284-0, 2014.

Wilheit, T. T.: A review of applications of microwave radiometry to oceanography, Boundary-Layer Meteorology, 13, 277–293, https://doi.org/10.1007/BF00913878, 1978.

Zine, S., Boutin, J., Font, J., Reul, N., Waldteufel, P., Gabarro, C., Tenerelli, J., Petitcolin, F., Vergely, J., Talone, M., and Delwart, S.: Overview of the SMOS Sea Surface Salinity Prototype Processor, IEEE Transactions on Geoscience and Remote Sensing, 15 https://doi.org/10.1109/TGRS.2008.915543, 2008.
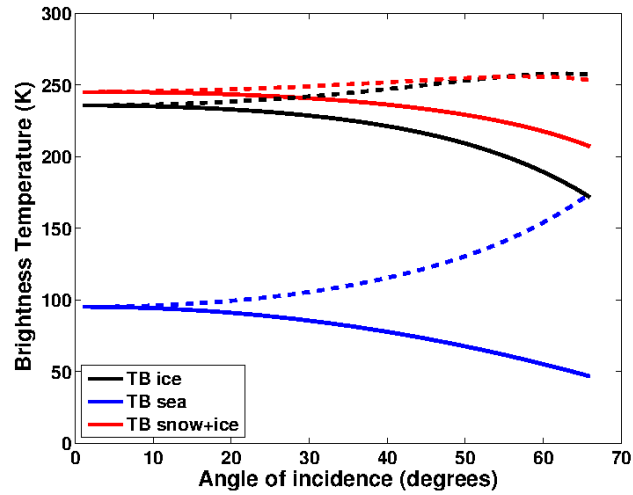
Figure 2. Theoretical variation of brightness temperature with angle of incidence at L-band for (blue) seawater, (black) sea ice, and (red) a snow layer overlying a sea ice layer for (continuous) horizontal and (dashed) vertical polarizations.
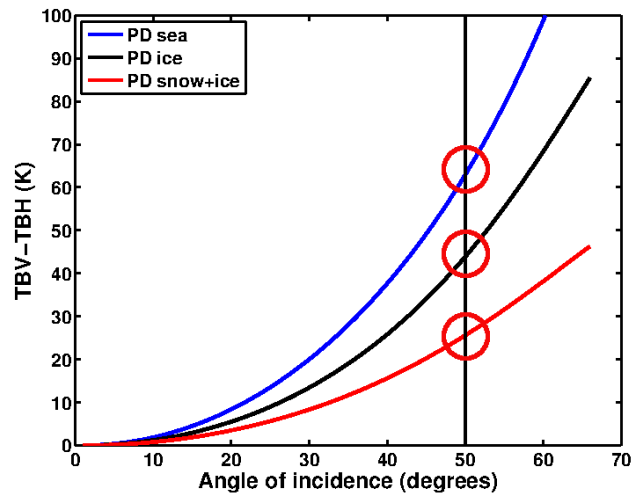
Figure 3. Modeled variation of polarization difference (PD) index with angle of incidence for (blue) seawater, (black) sea ice, and (red) a snow layer overlying a sea ice layer, at L-band. The vertical line at $50°$ incidence angle is drawn for reference to tie-points, which are marked with a solid circle for the three media.
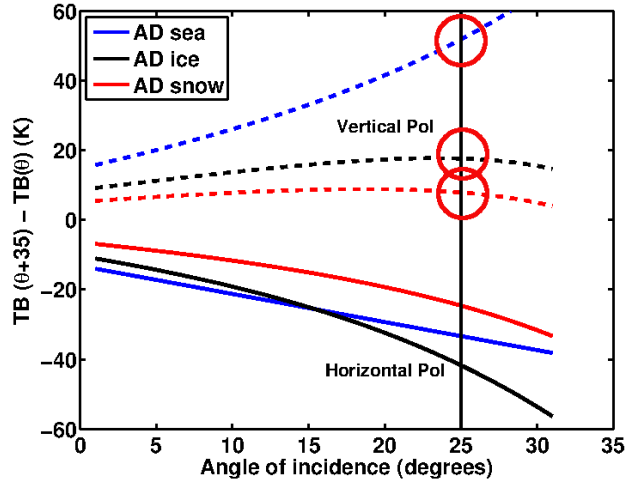
Figure 4. Modeled variation of angular difference index (AD) with angle of incidence for (blue) seawater, (black) sea ice, and (red) a snow layer overlying a sea ice layer for (continuous) horizontal and (dashed) vertical polarizations, and for $\Delta\theta = 35°$, at L-band. The vertical line at $25°$ incidence angle is drawn for reference to tie-points, which are marked with a solid circle on vertical polarization for the three media.
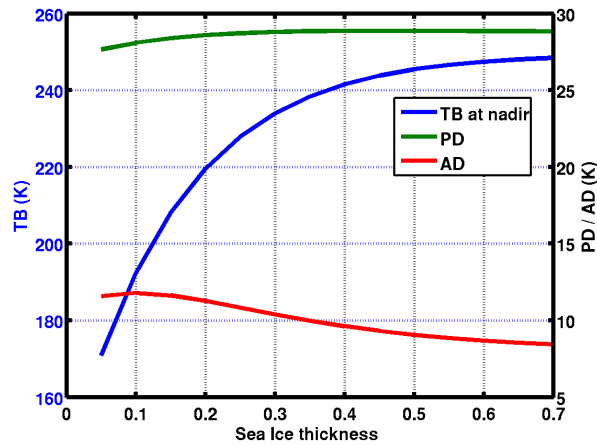
Figure 5. Theoretical variation with sea ice thickness of (blue; left axis) T_B at nadir, (green; right axis) polarization difference (PD) at $50°$ incidence angle, and (red; right axis) angular difference (AD) at $\Delta\theta = 25°$ after the model by Burke et al. (1979), for a sea ice salinity of 8 g/Kg, sea ice temperature of $-10°$ C, and a snow layer of 10-cm thick over the ice. Note the factor of 10 change between the left/right vertical scales.
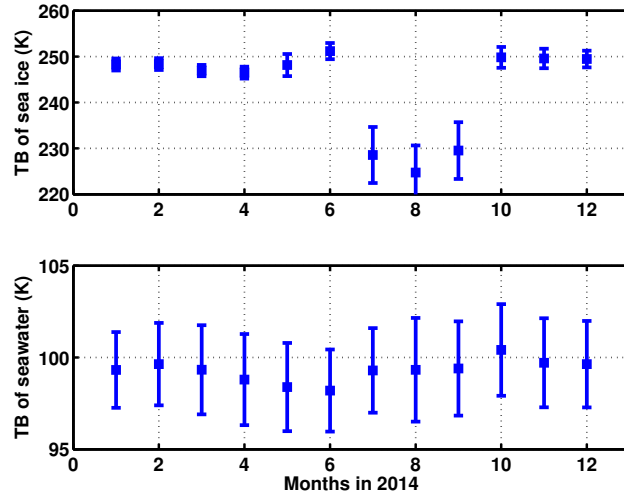
Figure 6. Temporal variation of the average brightness temperature T_B at nadir for (top) multy year sea ice and (bottom) seawater at the two regions for generating tie-points. Note the factor of 4 change in the vertical scales.
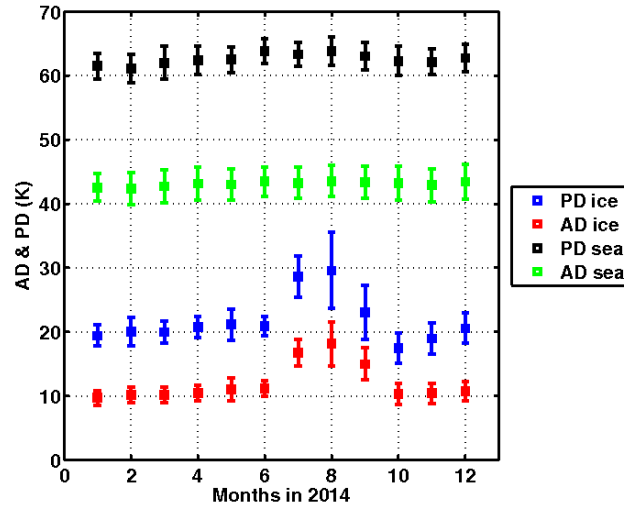
Figure 7. Same as Fig. 6 except here for angular and polarization difference indices.
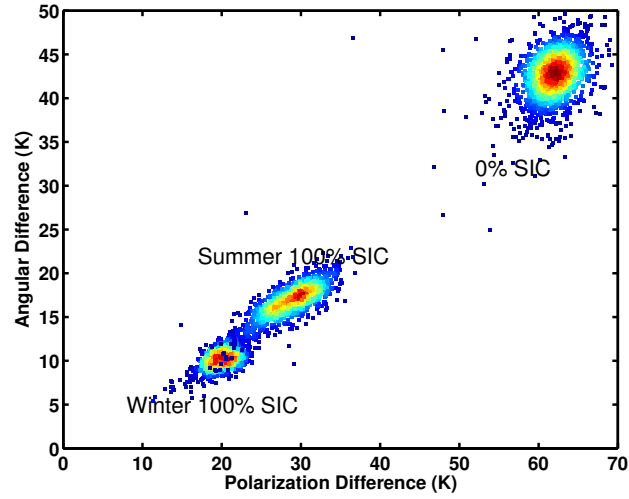
Figure 8. Scatter plot of the angular difference vs polarization difference in March and July 2014, with (red-to-blue) high-to-low index occurrence values for the two regions for generating tie-points, i.e., 0% and 100% sea ice concentration (SIC).
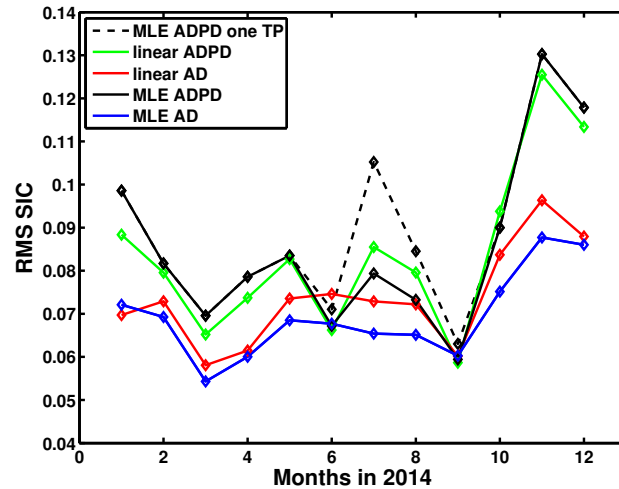
Figure 9. Comparison against OSI-SAF, of one tie-point (black dotted line) vs two tie-points (black plane line) with MLE; and MLE vs linear retrieval tecniques. If not defined in the labels it is two tie-points.
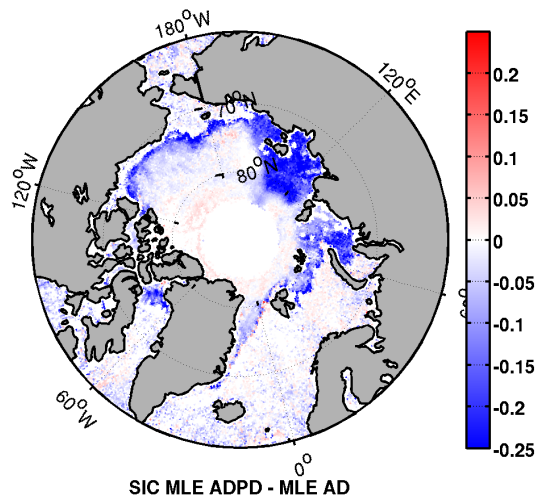
Figure 10. SMOS SIC with MLE AD+PD minus SMOS SIC with MLE AD inversion tecniques for 3rd November 2014. SIC scale is presented from 0 to 1.
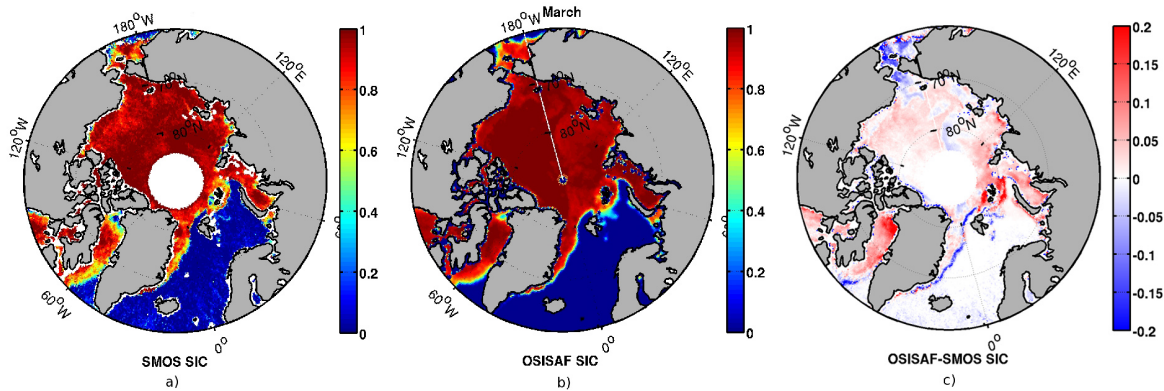
Figure 11. SMOS SIC with MLE (a), OSISAF SIC (b) and the differences (c) for 3rd March 2014.
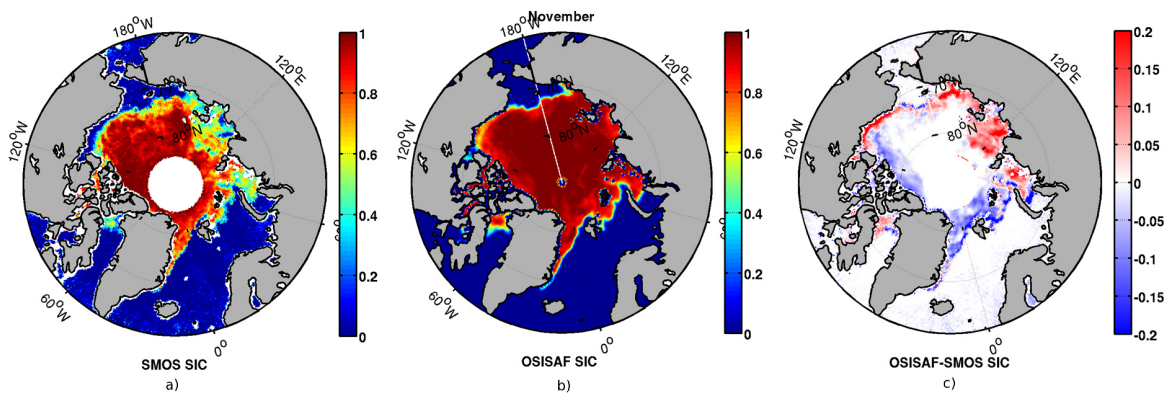
Figure 12. SMOS SIC with MLE (a), OSISAF SIC (b) and the differences (c) for 3rd November 2014.

Table 1. Modeled (with and without snow) and SMOS observed T_B, PD, and AD median values. Errors quoted are the standard deviation around the median.

		Modeled (K)		Observed all year median $\pm\sigma$ (K)	
0% SIC (Seawater)	T_B	95.2		99.33 ± 2.40	
	PD	62.9		62.56 ± 2.56	
	AD	51.8		43.08 ± 2.57	
		Modeled with snow (K)	Modeled without snow (K)	Observed Winter median $\pm\sigma$ (K)	Observed Summer median $\pm\sigma$ (K)
100% SIC (Sea Ice)	T_B	249.2	239.3	248.21 ± 1.56	229.04 ± 4.99
	PD	26.8	45.9	20.30 ± 1.75	25.53 ± 3.72
	AD	8.6	18.8	10.38 ± 1.17	15.26 ± 2.31
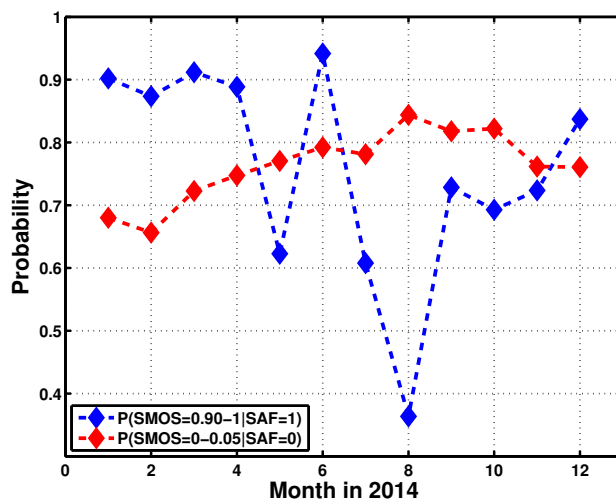
Figure 13. Probability to have SMOS SIC more than 0.90 where OSISAF SIC=1 (blue line) and SMOS SIC less than 0.05 where OSISAF SIC=0 (red line) for 2014. Summer tie-points are used for retrievals from June to September.
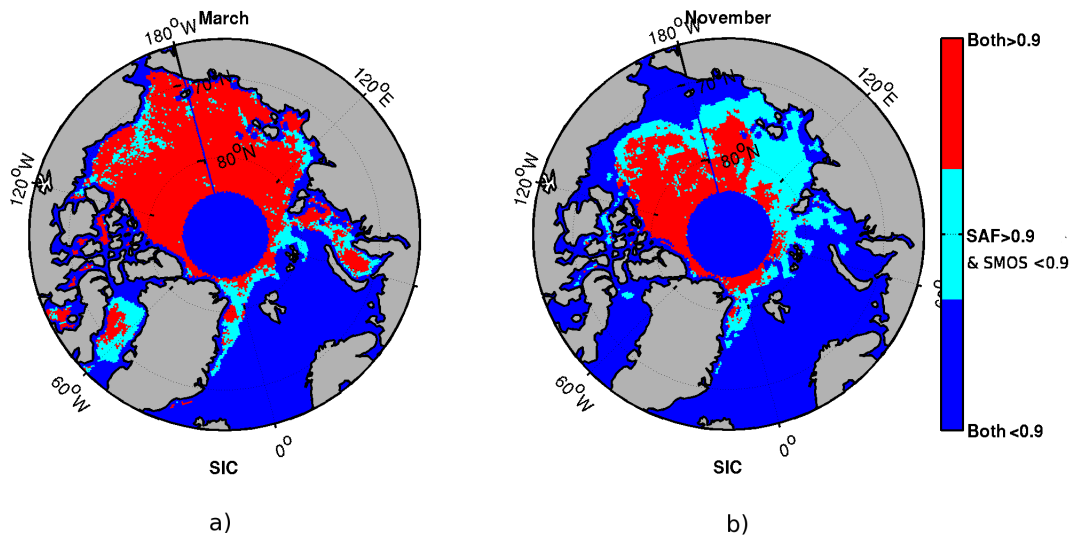
Figure 14. Classification of the Artic region according to their values of SMOS and OSI-SAF SIC during March (a) and November (b) 2014. Three classes are shown: 1) OSISAF $SIC < 0.9$; 2) OSISAF $SIC > 0.9$ and SMOS $SIC < 0.9$; and 3) OSISAF $SIC > 0.9$ and SMOS $SIC > 0.9$.
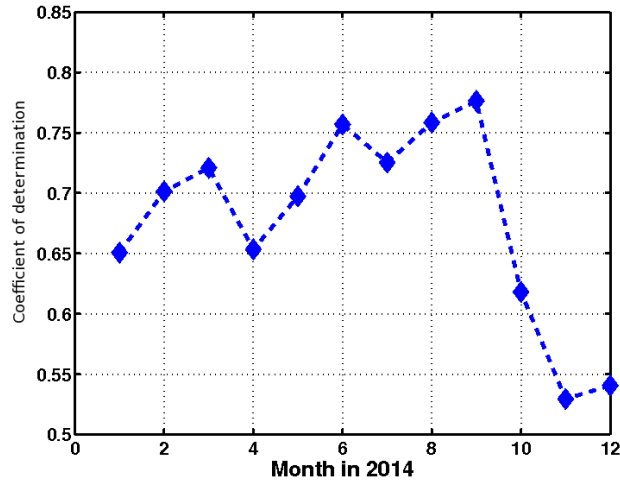
Figure 15. Coefficient of determination (R^2) between SMOS and OSISAF SIC for 2014, considering only SIC data in the range from 5% to 95%.

Table 2. Sensitivity of measurement T_B, PD, and AD to ice temperature (T), salinity (S), and thickness (d).

Medium	Index	$\delta I/\delta T$	$\delta I/\delta S$	$\delta I/\delta d$
	(I)	(K /° C)	(K / g/Kg)[1]	(K / cm)
	T_B	0.2	0.51	
Seawater	PD	0.26	0.21	
	AD	0.20	0.12	
	T_B	0.85	1.00	1.2
Sea ice	PD	0.66	0.35	0.02
	AD	0.35	0.25	0.05

[1] practical salinity units

Table 3. Propagated SIC error using each index, computed from Eq. 12 for assumed (T, S, d) variations, and root-sum-squared (RSS).

SIC error	index	ΔT	ΔS	Δd	RSS
(%)	used	5 K	4 g/Kg	30 cm	
ΔSIC	TB	2.8	2.6	23.4	23.7
ΔSIC	PD	7.6	3.2	1.4	8.3
ΔSIC	AD	4.8	2.8	4.2	7.0